

See discussions, stats, and author profiles for this publication at: <https://www.researchgate.net/publication/303563271>

Developing terahertz imaging equation and enhancement of the resolution of terahertz images using deconvolution

Conference Paper · May 2016

DOI: 10.1117/12.2228680

CITATIONS

2

READS

17

2 authors:



Kiarash Ahi

University of Connecticut

49 PUBLICATIONS 38 CITATIONS

SEE PROFILE



Mehdi Anwar

University of Connecticut

169 PUBLICATIONS 957 CITATIONS

SEE PROFILE

Developing Terahertz Imaging Equation and Enhancement of the Resolution of Terahertz Images using Deconvolution

Kiarash Ahi, Mehdi Anwar
Department of Electrical and Computer Engineering
University of Connecticut
371 Fairfield Way, Storrs, CT 06269, United States
kiarash.ahi@uconn.edu, a.anwar@uconn.edu

ABSTRACT

This paper introduces a novel reconstruction approach for enhancing the resolution of the terahertz (THz) images. For this purpose the THz imaging equation is derived. According to our best knowledge we are reporting the first THz imaging equation by this paper. This imaging equation is universal for THz far-field imaging systems and can be used for analyzing, describing and modeling of these systems. The geometry and behavior of Gaussian beams in far-field region imply that the FWHM of the THz beams diverge as the frequencies of the beams decrease. Thus, the resolution of the measurement decreases in lower frequencies. On the other hand, the depth of penetration of THz beams decreases as frequency increases. Roughly speaking beams in sub 1.5 THz, are transmitted into integrated circuit (IC) packages and the similar packaged objects. Thus, it is not possible to use the THz pulse with higher frequencies in order to achieve higher resolution inspection of packaged items. In this paper, after developing the 3-D THz point spread function (PSF) of the scanning THz beam and then the THz imaging equation, THz images are enhanced through deconvolution of the THz PSF and THz images. As a result, the resolution has been improved several times beyond the physical limitations of the THz measurement setup in the far-field region and sub-Nyquist images have been achieved. Particularly, MSE and SSIM have been increased by 27% and 50% respectively. Details as small as 0.2 mm were made visible in the THz images which originally reveals no details smaller than 2.2 mm. In other words the resolution of the images has been increased by 10 times. The accuracy of the reconstructed images was proved by high resolution X-ray images.

Keywords: Resolution enhancement, THz imaging equation, deconvolution, physical inspection, quality control

1. INTRODUCTION

Traditionally generation and detection of electromagnetic radiation in terahertz (THz) were not commercially available until a few decades ago ¹. Unlike X-ray imaging which has been used more than a century, first THz image has been developed less than two decades ago ². X-ray imaging equations have been formulized well but no imaging equation has been developed for THz imaging systems ³. According to our best knowledge we are reporting the first THz imaging equation. The first purpose of the work was enhancement of the resolution of terahertz images. Since there were no imaging equations reported in the literature we had to develop THz imaging equation first. This imaging equation is universal for THz far-field imaging systems and can be used for analyzing, describing and modeling of THz imaging systems.

Electromagnetic beams in THz region are capable of penetrating nonconductive materials. THz region of radiation is commonly refers to 0.1 to 10 THz in the literature, and lies in the gap between electronic and optical signal generation schemes or in other words between microwave and infrared. Microwaves have the ability to penetrate composites as well. But in this case, lower resolution would be achieved due to their longer wavelengths of microwaves compared to THz. Although infrared radiation has shorter wavelength and would give better resolution, it provides less penetration depth compared with THz ⁴. Conventionally, X-ray transmission imaging and scanning acoustic microscopy (SAM) has been used for inspection of packaged objects. SAM imaging requires the object to immerse in a liquid, usually water,

and thus it can damage the object. Moreover the frequency of the acoustic waves in SAM techniques are less than GHz and thus the achieved resolution would be less than THz images⁵. To keep up with Moore's law, semiconductor devices are constantly being scaled. Scaled devices with lower oxide/insulation barriers are more vulnerable for ionization effects of X-ray. As a specific example, energies of X-rays photons are in the range of 100 eV to 100 keV, while the electric barriers in flash memories are less than 5 eV. Consequently, using X-rays causes the data on flash memories to be disrupted^{6,7}. It does not limit to flash memories, diodes and transistors are also susceptible to ionizing radiation. Here, the thicker of the gate oxide, the more vulnerable the devices to X-ray. The latter phenomenon is due to the fact that the absorbed dose is higher for the thicker devices. Ionization causes parameter degradation or permanent damage of the devices, and could cause catastrophic failures of machinery in which the defected devices are used⁸. Unlike X-ray, THz has non-ionizing photon with low energies (0.4-40 meV)⁹. THz radiation is not ionizing, and thus it is nondestructive for electronic devices, medicines and safe for live tissues. Many materials in THz spectral region have unique spectral fingerprints, consequently, THz techniques can be used for determining the materials in wide variety of objects from medicines to electronic components^{10,11}. These characteristics make THz a promising option for inspections¹²⁻¹⁴. In general, compared to other inspection techniques, THz inspection techniques have the privilege to be nondestructive, nonhazardous, less human dependent, economical and faster.

Although THz combines the high penetration depth of microwaves together with submillimeter spatial resolution, still the shortcoming of the THz imaging and spectroscopy, compared to X-ray imaging, is its low resolution¹⁵. Geometry and behavior of Gaussian beams in Fraunhofer region imply that the electromagnetic beams diverge more as the frequencies of the beams decrease and thus the resolution decreases^{3,4,16}. Particularly, at 1 THz, the far-field spatial resolution of an image is restricted to the Rayleigh criterion which corresponds to 180 μm in vacuum¹⁷. On the other hand, the depth of penetration of THz beams decreases as frequency increases, because the higher frequencies tend to get more absorbed in materials¹⁵. Absorption characteristic of THz beam is shown in Figure 1-(a) while passing through a 2.3 mm packaged IC. As it is shown in Figure 1-(b), it's the lower frequencies, roughly speaking sub 1.5 THz that are transmitted into materials of IC packages and can be used for inspection purposes. Consequently, a trade-off between the depth of penetration and the resolution has to be taken for inspection techniques. This limits THz capabilities.

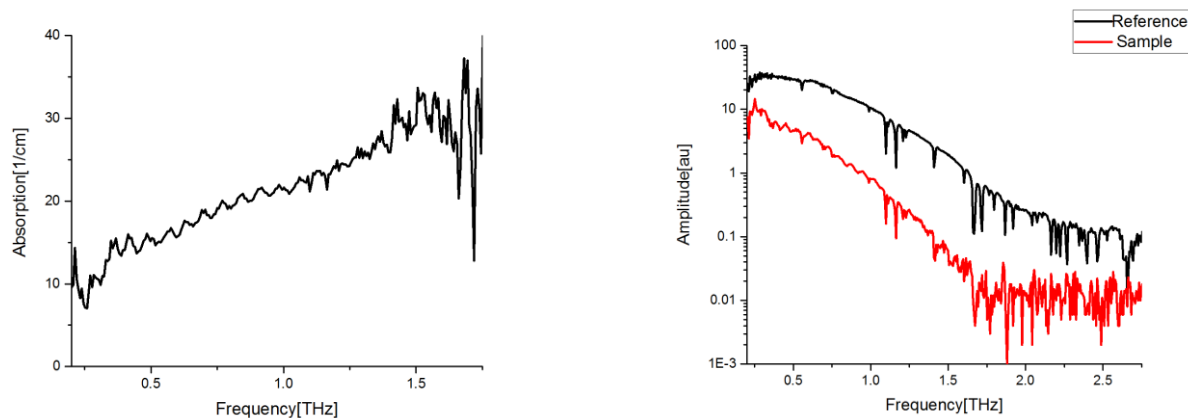


Figure 1 THz spectrum of transmitted beam from a 2.3 mm IC package; a) Absorption increases exponentially with respect to frequency; b) Frequencies higher than 1.5 THz are not basically transmittable in the packaged IC.

Near-field THz microscopy techniques have been introduced as an alternative application of THz imaging and a solution to the limited resolution of THz systems in far-field region¹⁸⁻²¹. THz microscope with resolutions of 14 μm at centered frequency of 0.7 THz are realized¹⁷. Imaging of terahertz surface plasmon waves and active electric near field imaging of electronic devices has been reported^{22,23}. In another trend, a laser terahertz emission microscope (LTEM) using a 10 THz laser beam, with a pulse width of 100 fs, is developed by Kiwa and Tonouchi²⁴. The laser beam is used to irritate the p-n junctions of electronic chips and as a result a THz radiation, in the range of 1 THz, is generated from the unbroken connections. In this way the open defects can be distinguished wherever no THz radiation is observed. The authors of the mentioned work have reported that spatial resolutions of the images were not sufficient to localize the

scratches. For improving the latter approach, in more recent works, Nikawa *et al.* have used laser beams with 30 THz and achieved higher resolutions is achieved²⁵. But again it should be noted that the beam in high THz frequencies would be absorbed in the packaged materials of ICs. Moreover, this method can only locate the p-n junctions in the chip and a full image of the inside of the packaged ICs cannot be obtained.

In this paper, instead of increasing the frequency of the THz beam physically, mathematical approaches are developed to increase the resolutions of the THz images. The idea is based on the fact that the THz images are constructed as the result of the raster scan of the objects by THz beam. In this work, this THz beam was considered to be the point spread function (PSF) which is convolved with the object. The result of this convolution is the THz image. Consequently, deconvolution of the resulted image and the beam can give a better representation of the object. But for achieving this aim, the PSF should be known. The equation of this three dimensional PSF is developed based on the physical characteristics of the terahertz beam. In section-II, mathematical equation for this PSF is derived and THz imaging equation is developed. In section-III, an approach for the described deconvolution is developed. Finally section-IV, demonstrate the results and gives the metrics for enhancement of the THz images.

2. DEVELOPING THE POINT SPREAD FUNCTION OF THE THZ BEAM

A. Basic Imaging Concepts

In a typical THz imaging system an image is obtained by raster-scanning the target under the focal plane of the focusing objective lenses. Figure 2 shows THz imaging system, in University of Connecticut, where the x - y plane represents the raster coordinate of the imaging system. The output of such imaging system is the convolution of the PSF of that system and the object function. The image also contains additive noise²⁶. Equation-1 represents the output of an imaging system mathematically.

$$s(x, y) = PSF(x, y) * o(x, y) + n \quad (1)$$

Where, s is the obtained image and o is object function. For the THz transmission imaging systems, the obtained image would represent the superimposed images of all the images of the object upon the convolution of the PSF and the object function at $z=z_i$. Where z is the axis from the THz transmitter, located at $z=z_t$ to the THz detector at $z=z_d$.

$$s(x, y) = \int_{z_t}^{z_d} \int_{x'} \int_{y'} o(x - x', y - y', z_i) PSF(x', y', z_i) dx' dy' dz \quad (2)$$

It should be taken into consideration that the THz pulse is not a single frequency beam. As Figure 3 illustrates the spectrum of the pulse, it is consisting of frequencies expanded from a few hundred GHz to several THz. Consequently for reconstruction of the THz beam, superposition of Gaussian beams with respect to the mentioned frequencies is to be considered.

$$PSF = \int PSF(\omega) d\omega \quad (3)$$

B. Modeling of the THz PSF by Gaussian Beams Concepts

It has been shown by Jepsen *et al.* that the terahertz beam can be represented by a Gaussian beam²⁷. The source device used in the system is considered as a circular aperture lens-coupled antenna which output can be approximated by Gaussian illumination distribution²⁸. After exiting the circular aperture and cylindrical lenses of the imaging system, this Gaussian illumination distribution remains Gaussian. Larger truncation ratios, W , gives smaller PSF sizes but the side lobes will be larger which may be resulted in the flared images²⁹. For avoiding this problem, the aperture in our system is chosen to achieve the $W \approx 1$. In addition, although in near-field an aperture Gaussian beam have a complex irradiance profile characterized by rapid intensity fluctuations across the transverse coordinate, in the far field, the irradiance pattern typically consists of a main central lobe and much smaller intensity oscillations in the wings. For $W=1$, fraction of the central lobe power for a circular aperture is reported to be more than 95% of the total beam power³⁰.

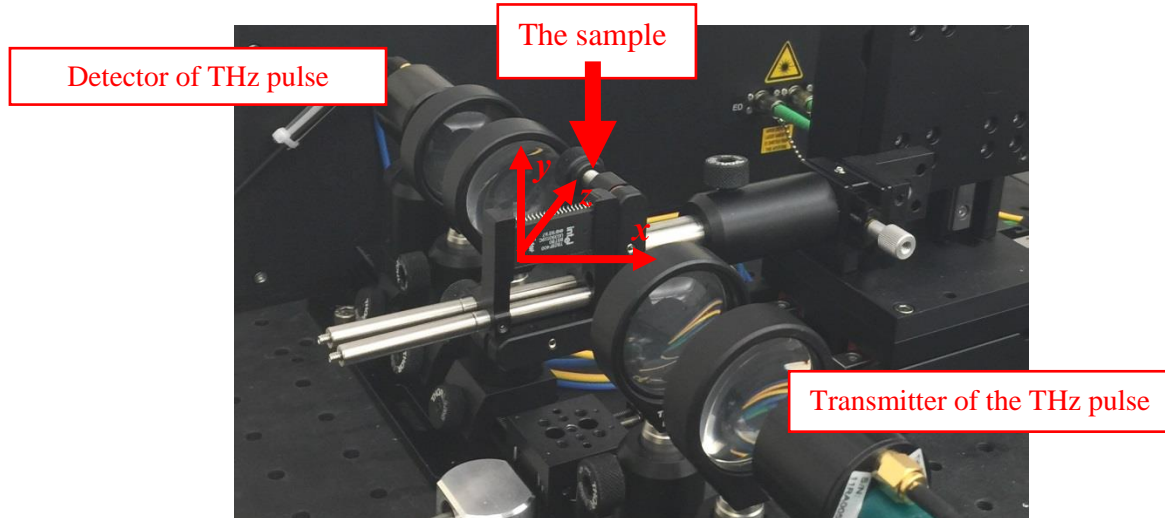


Figure 2 The experimental setup in reflection mode. The red laser spot is used to mark the location of the THz beam

Consequently, the oscillations in the wings can be neglected compared to the main lobe and the THz beam which shapes the PSF of the THz imaging system can be approximated by a TEM_{00} mode Gaussian beam with 10° divergence or roughly speaking by a single Gaussian distribution.

The spot size boundary of the Gaussian beam is defined to be where the intensity drops to $1/e^2$ of the peak value of the beam intensity. The radius of the spot at distance z from the beam waist is given by Equation-4³¹.

$$w(z) = w_0 \sqrt{1 + \left(\frac{\lambda z}{\pi w_0^2}\right)^2} \cong \frac{\lambda z}{\pi w_0} = \frac{c}{\pi w_0} \left(\frac{z}{f}\right) = \Lambda\left(\frac{z}{f}\right) \quad (4)$$

Where w_0 is the spot radius at the waist and λ is the wave length. Denoting the factor $\frac{c}{\pi w_0}$ by ν^{-1} gives:

$$\nu w(z) = \frac{z}{f} \quad (5)$$

The intensity profile of the THz beam then can be represented by the following Gaussian function.

$$I(r) = I_0 e^{-2r^2/w(z)^2} \quad (6)$$

Where I_0 is the intensity at the center of the beam. For the above Gaussian distribution, the full width at half maximum (FWHM) is calculated by Equation-7.

$$FWHM = w(z) \sqrt{2 \ln 2} \quad (7)$$

On the other hand, $FWHM$ of a diffraction limited focused spot is given by Equation-8.

$$FWHM = \frac{k\lambda}{NA} \quad (8)$$

Where k is the k-factor of the truncated Gaussian regime, and depends on the truncation ratio W and the level of irradiance in the image spot used to measure the diameter of the image and NA is numerical aperture³². Substituting Equation-8 into Equation-7 gives $w(z)$ and then by using Equation-6, the beam profile can be obtained.

$$r = w(z) = \frac{FWHM}{\sqrt{2 \ln 2}} \quad (9)$$

The divergence angle of the beam, θ , is given by Equation-10³³.

$$\theta = \frac{\lambda}{\pi w_0} \quad (10)$$

Where w_0 is in millimeter, λ is in meter and θ in radian.

C. Incorporating of the Transmission Concepts and Absorption of the Objects into the Imaging Equation

Unlike optical imaging systems, transmission THz imaging systems develop images based on the measured attenuation of the THz beam as passing through the object. This attenuation is caused by three factors, namely, absorption, reflection and scattering of the THz beam in reaction with the object. Denoting the magnitude of the power of the transmitted THz beam at the transmitter point by P_t , absorbed power by the materials between the transmitter and the receiver by P_a , scattered beam by P_s and reflected beam by P_r , the detected power at the THz detector is obtained by Equation-11.

$$P_d = P_t - P_a - P_s - P_r \quad (11)$$

By including time, t , Equation-11 could be represented more specifically by the received, $E_r(t)$, and transmitted, $E_t(t)$, signals and the transfer function of the object. The transfer function is a function of the thickness of the slab, T , its refractive index, n , and its extinction coefficient, k ³⁴. Taking the travel time of the reference signal between the THz transmitter and the detector by $p = (d - T) / c$, where d is the distance between the THz transmitter and the detector, $d = z_t - z_d$, and c is the speed of light in the air, Equation-12 is obtained.

$$E_d(t) = E_t(t - p) * T(t, T, n, k) \quad (12)$$

Using the representation of received signal, E_d , in Equation-12, the THz PSF in THz imaging equation (Equation-2) can be obtained. First it is needed to be analyzed that which portion of the received signal is contributing to the image formation. Here, we consider the sample to be “optically thick”, meaning that the sample is thick enough that the THz signal falls to zero between two echoes inside the sample and thus the first directly transmitted pulse and higher order echoes are well separated at the detector point³⁵. The frequency domain representation of the Equations-12 is given by Equation-13.

$$E_d(\omega) = E_t(\omega) \exp(-j\omega \tilde{n}_s p) \times T(\omega) \quad (13)$$

Where:

$$T(\omega) = \frac{T_{as}(\omega) T_{sa}(\omega) \exp(-j\omega \tilde{n}_s T / c)}{1 + \Gamma_{as}(\omega) \Gamma_{sa}(\omega) \exp(-2j\omega \tilde{n}_s T / c)} \quad (14)$$

In the latter Equation, $\tilde{n}_s = \tilde{n}_s - jk_s$, is the complex refractive index of the sample depends on the angular frequency ω , $T_{as}(\omega)$ and $T_{sa}(\omega)$ are respectively transmission coefficient from the air to the sample and vice versa, $\Gamma_{as}(\omega)$ and $\Gamma_{sa}(\omega)$ are respectively reflection at the air to the sample interface and vice versa³⁵.

$$T_{as}(\omega) = \frac{2\tilde{n}_s}{\tilde{n}_a + \tilde{n}_s} \quad (15)$$

$$\Gamma_{as}(\omega) = \frac{n_a - n_s}{\tilde{n}_a + \tilde{n}_s} \quad (16)$$

With $\Gamma_{as}(\omega) = -\Gamma_{as}(\omega)$, $T_{as}(\omega) = 1 - \Gamma_{as}(\omega)$ and $T_{sa}(\omega) = 1 + \Gamma_{as}(\omega)$.

Expanding Equation-14 using binomial series, substituting it into Equation-13 and taking its reverse Fourier transform gives Equation-17.

$$\begin{aligned} E_d(t) = & \left[E_t(t-p) * T_{as}(t) * T_{sa}(t) * f_s(t) \right] u(t-\tau_s) \\ & - \left[E_t(t-p) * T_{as}(t) * T_{sa}(t) * \Gamma_{as}(t) * \Gamma_{sa}(t) * f_s^3(t) \right] u(t-3\tau_s) + \dots \end{aligned} \quad (17)$$

Where $f_s(t)$ is the time-domain dispersion function resulted by the one-way propagation in the sample. In Equation-17 the first directly transmitted pulse and higher order echoes are well analyzed. Each of these echoes could be also used for constructing images. Figure-3 has obtained from having a 2.3 millimeter thickness packaged IC. This IC is considered an optically thick sample. In Figure-3-(a) the time delays of the echoes clearly confirm time delays in Equation-17. Obviously the magnitude of the first directly transmitted pulse is higher than echoes. It is less scattered and less diffracted. Consequently, for developing THz images only the first directly transmitted pulse is used in this work. For modeling the PSF first directly transmitted pulse will be taken into account as well. Calling the first term in Equation-17 as E_{d1} , Equation-18 can be written.

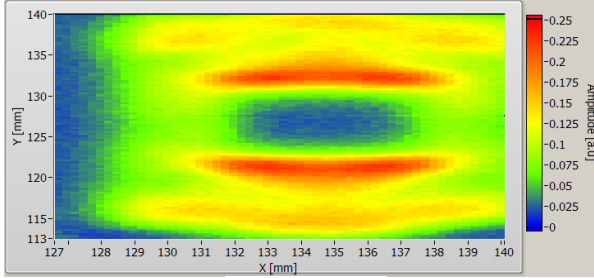
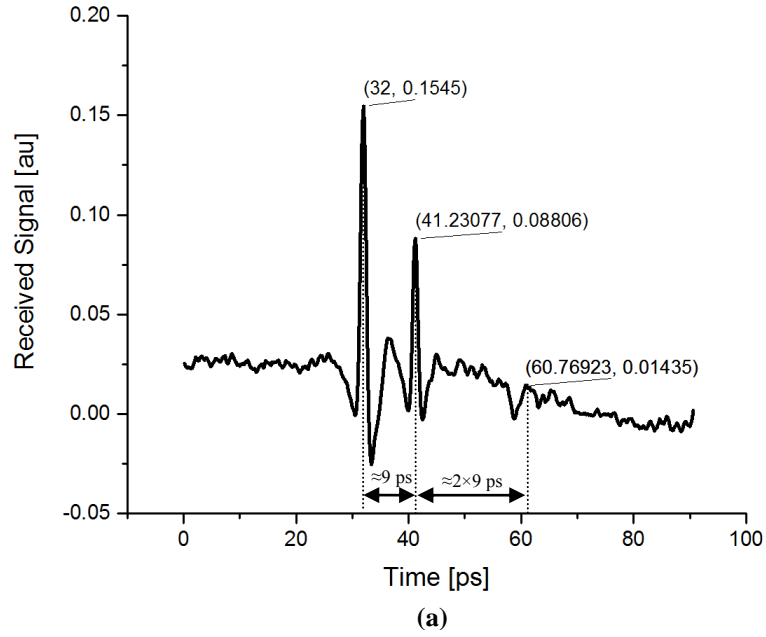
$$E_{d1}(t) = E_d(t) - \sum_{i>1} E_{di}(t) \quad (18)$$

Substituting $E_d(t)$ from Equation-12 into Equation-18 yields:

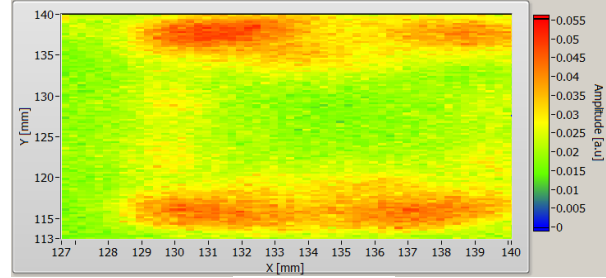
$$E_{d1}(t) = E_t(t) - E_r(t) - E_s(t) - \sum_{i>1} E_{di}(t) \quad (19)$$

Where E_r is the reflected signal and E_{di} terms are the detected echoes. $E_r(t)$ and $E_s(t)$ do not reach the THz detector. Due to distinct time delays of the echoes and the first directly transmitted pulse, $E_d(t)$, for optically thick samples, echoes can be filtered easily. After applying this time filtering and neglecting the effects of the ambient air, $E_t(t-p)$ can be considered the reference signal $E_{ref}(t)$. Reference signal is defined the detected signal where no material is placed between the transmitter and the detector. This signal is shifted by p due to the fact that reference signal is measured at the THZ detector while E_t was considered at the transmitter:

$$\begin{aligned} E_t(t) = E_{d1}(t) = & \left[E_t(t-p) * T_{as}(t) * T_{sa}(t) * f_s(t) \right] \\ = & \left[E_{ref}(t) * \mathcal{G}(t) \right] \end{aligned} \quad (20)$$



(b)



(c)

Figure 3 (a) Time delays of the echoes; (b) The directly transmitted pulse (c) The first echo.

Taking the Furrier transform of the latter Equation, gives the frequency domain representation of the imaging pulse:

$$E_i(\omega) = E_{ref}(\omega) \mathcal{G}(\omega, z) \quad (21)$$

On the other hand on z axis we have:

$$\alpha_s(\omega) = -\frac{1}{z} \ln \frac{E_i(\omega, z)}{E_{ref}(\omega)} = -\frac{1}{z} \ln \mathcal{G}(\omega, z) \quad (22)$$

Where α_s is the absorption coefficient of the sample and has the units of cm^{-1} . Merging the last two equations yields:

$$E_i(\omega, z) = e^{-z\alpha(\omega)} E_{ref}(\omega) \quad (23)$$

Incorporating the terahertz Gaussian beam profile from Equation-6 into Equation-23 yields:

$$PSF(\omega, z) = E_{ref}(\omega) e^{-(z\alpha(\omega) + 2r^2/w(z)^2)} = E_{ref}(\omega) e^{-(z\alpha(\omega) + 2(r\pi w_0/\lambda z)^2)} \quad (24)$$

Substituting $w(z)$ from Equation-5 into the last equation yields:

$$PSF(\omega, z) = E_{ref}(\omega) e^{-(z\alpha(\omega) + 2(r\pi w_0/\lambda z)^2)} = E_{ref}(\omega) e^{-(z\alpha(\omega) + 2(2r\pi^3 w_0 \omega / cz)^2)} \quad (25)$$

Representing the last Equation in discrete form gives Equation-26.

$$PSF(\omega, z) = \sum_{\omega_i} E_{ref}(\omega_i) e^{-(z\alpha(\omega_i) + 2(2r\pi^3 w_0 \omega_i / cz)^2)} \quad (26)$$

Substituting the last Equation into Equation-1 gives the THz imaging equation.

$$s(x, y) = \sum_{\omega_i} E_{ref}(\omega_i) e^{-(z\alpha(\omega_i) + 2(2r\pi^3 w_0 \omega_i / cz)^2)} * o(x, y, z) \quad (27)$$

The absorption coefficient, which appeared in the latter equation, is calculated as following³⁶.

$$\alpha_s(\omega) = \frac{2}{T} \ln \left(\frac{4n_s(\omega)}{\rho(\omega)(n_s(\omega) + 1)^2} \right) \quad (28)$$

Where $\rho(\omega)$ is the magnitude of the ratio of the reference, $E_r(\omega)$, and imaging signal, $E_i(\omega)$.

$$\rho(\omega) = \left| \frac{E_i(\omega, z)}{E_{ref}(\omega)} e^{-j\phi(\omega)} \right| = \frac{|E_i(\omega, z)|}{|E_{ref}(\omega)|} \quad (29)$$

Using Equation-24, the PSF of the system can be modeled at each point on z axis inside the sample.

3. ENHANCEMENT OF THE RESOLUTION OF TERAHERTZ IMAGES

The THz image is obtained as the result of the raster scanning of the object by the focused THz beam as shown in Figure-2. As Equation-1 implies a THz image is the result of convolution of the object and the THz PSF. Consequently, deconvolution of the PSF and the THz image could give a higher resolution representation of the object.

$$o(x, y) = \text{deconv}(PSF(x, y, z, \omega), s(x, y)) \quad (30)$$

For this aim, first the THz PSF needs to be modeled. Using Equation-24, the PSF of the system is modeled at each point on z axis inside the sample. The THz beam is focused at the surface of the sample and thus the radius of the beam is equal to the waist of the beam, w_0 , on the surface of the sample. The waist of the beam is calculated by Equation-10, and it converges inside the sample according to the Equation-24. In addition to z , PSF in Equation-24 depends on frequency of the beam. The spectrum of the reference signal is calculated using Fourier transform, as shown in Figure-4. The overall PSF is the weighted superposition of the PSFs with different frequencies.

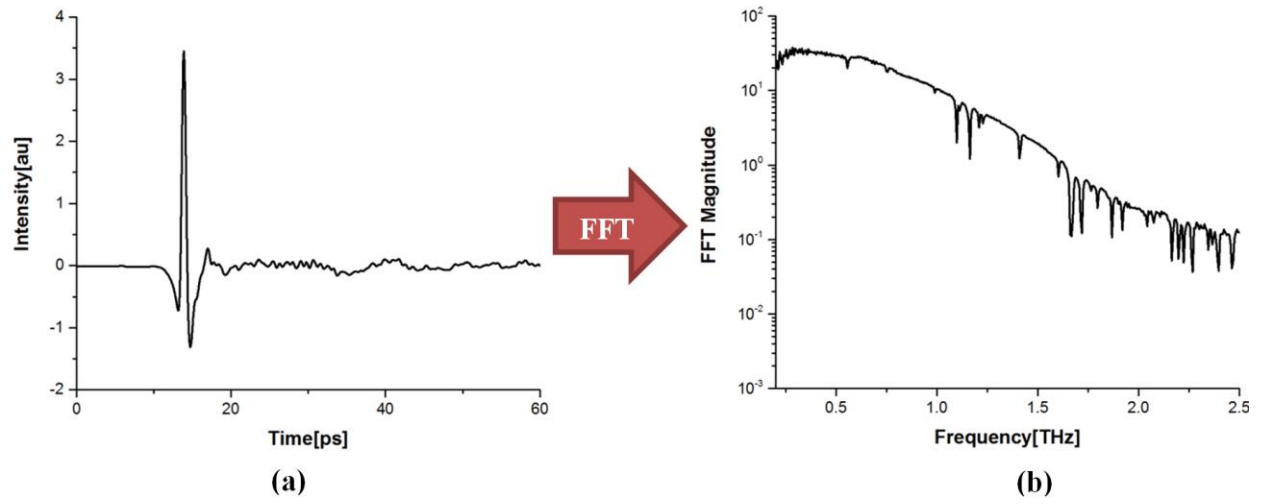


Figure 4 (a) The reference signal, $E_{ref}(t)$; (b) The magnitude of the spectrum of reference signal $E_{ref}(\omega)$

In addition, The THz PSF in Equation-24 depends on absorption coefficient of the sample. Absorption coefficient is also a function of frequency. The absorption coefficient is given by Equation-28. The absorption coefficient of a 2.3mm thick packaged IC, which is used as the sample in this work, is calculated and shown in Figure-5.

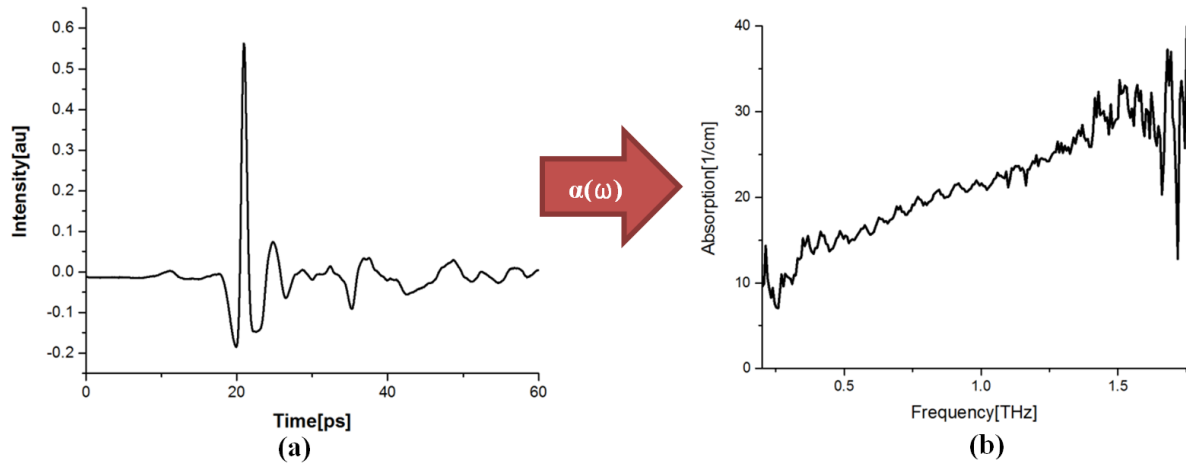


Figure 5 (a) The THz signal after passing through the sample, $E_i(t)$; (b) The absorption coefficient of the sample $\alpha(\omega)$

The corresponding absorption at each frequency is calculated using Equation-28 and is substituted in PSF equation. The normalized focused PSF is shown in Figure-4, the parameters of the system are $NA=0.3519$, $f\#=1.4211$, *pupil diameter*=38mm, *focal length*= 54 mm, *wavelength*=0.6mm, *rim intensity at the lens* %0.0001, *k-factor* 1.09 and *truncation loss*= %0.0001. Using Equations 4-10 and the following notation, the radius of the Gaussian function and the standard deviation, is calculated to be $FWHM=1.9mm$, e^2 *diameter*= $d=3.2$ mm or 100 pixels and $\sigma=0.806$ mm or 25 pixels.

$$d = \frac{2FWHM}{\sqrt{2\ln 2}} = \frac{FWHM}{0.589} \quad (31)$$

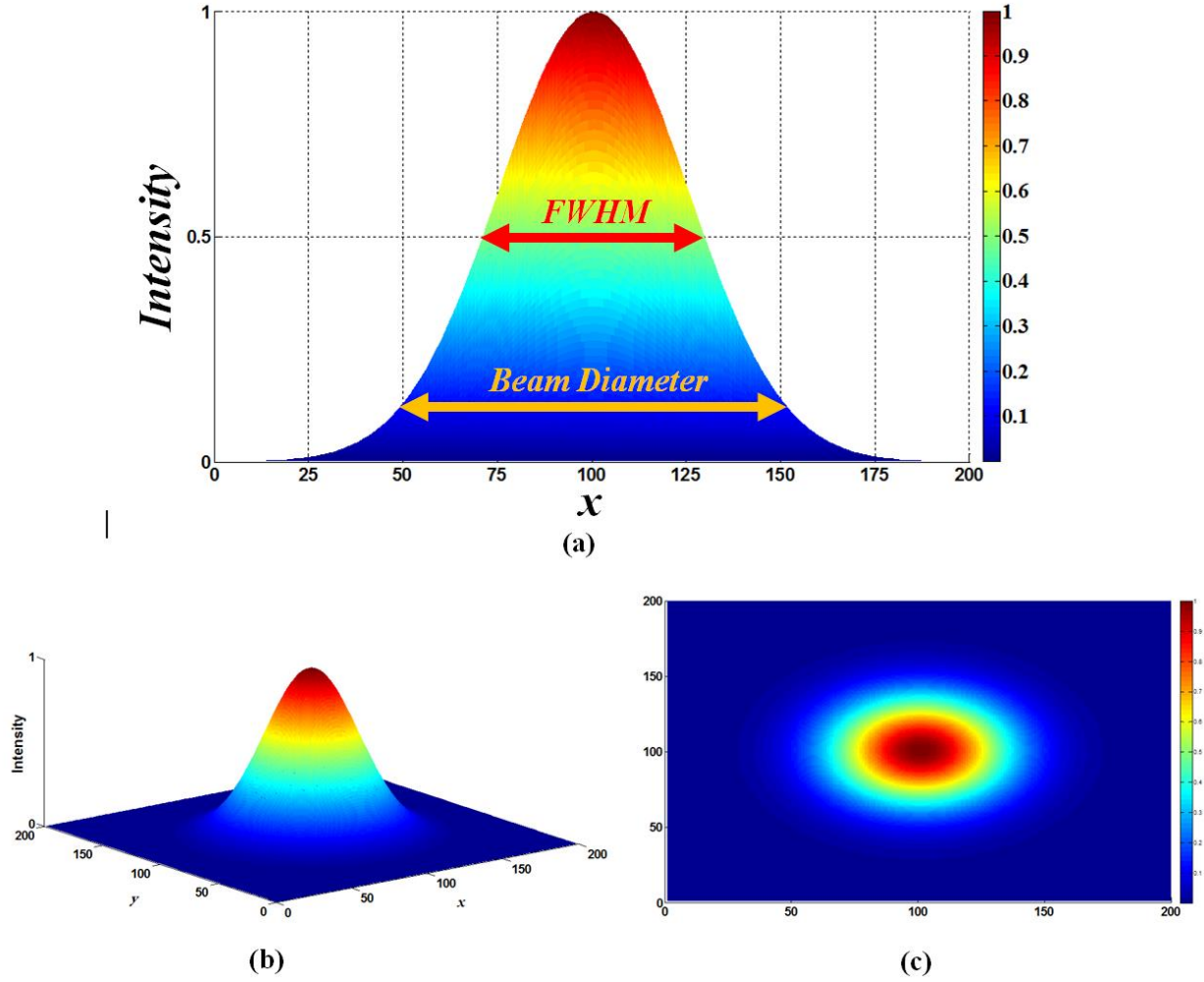
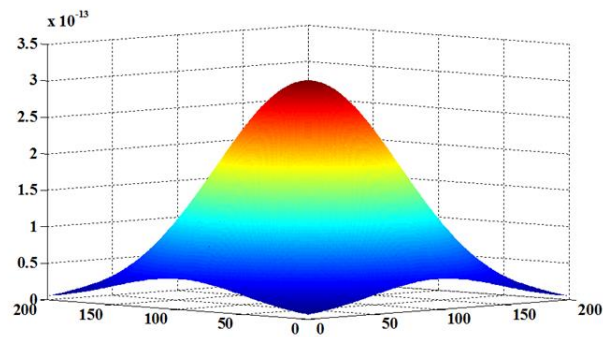


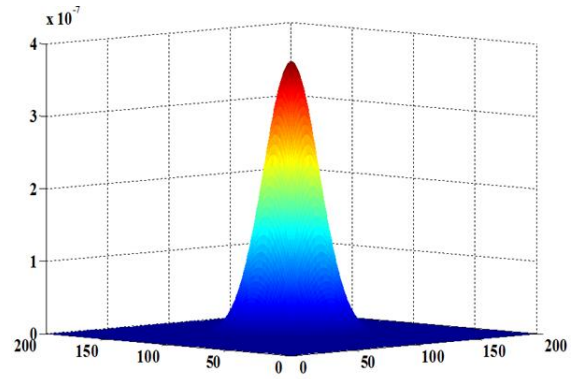
Figure 6 The normalized focused PSF, for the described THz system: (a) FWHM and e^2 diameter are denoted on the beam pattern; (b) Beam pattern as a 2-D Gaussian function; (c) The intensity profile of the beam pattern

$$\sigma = \frac{r}{2} = \frac{d}{4} \quad (32)$$

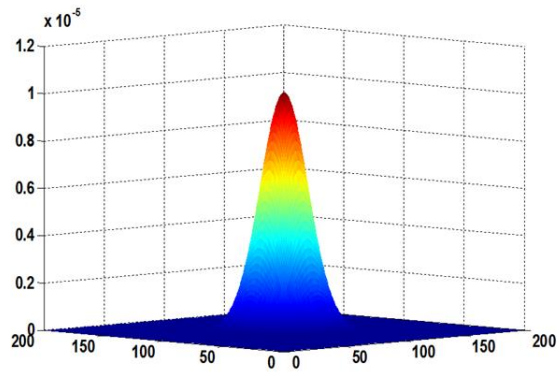
In Figure-7-(a) and (b) the exponential term for $f_i = 0.3 \text{ THz}$ and $f_i = 1 \text{ THz}$ of the THz PSF equation, Equation-24, is shown. According to the THz PSF equation, the terms with higher frequencies are suppressed exponentially with frequency and absorption. That's why the corresponding term for $f_i = 1 \text{ THz}$ is very smaller than corresponding term for $f_i = 0.3 \text{ THz}$. The THz PSF, which is the super-positioned THz PSFs of all the ω_i s, is illustrated in Figure-7-(c) and (d) for $z = \text{waist}$.



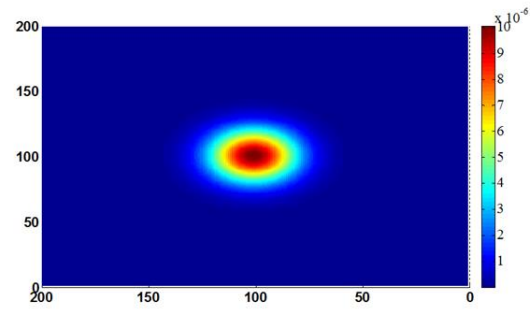
(a)



(b)



(c)



(d)

Figure 7 a) The exponential term for $f_i = 0.3 \text{ THz}$ and b) for $f_i = 1 \text{ THz}$ of the THz PSF equation; c) Super-positioned THz PSF; d) Super-positioned THz PSF from above

As z increases from the waist, the beam diverges and suppresses according to Equation-4 and THz PSF equation, respectively. Using Equation-24 the divergence and suppression of the beam over z -axis are illustrated in Figure-8.

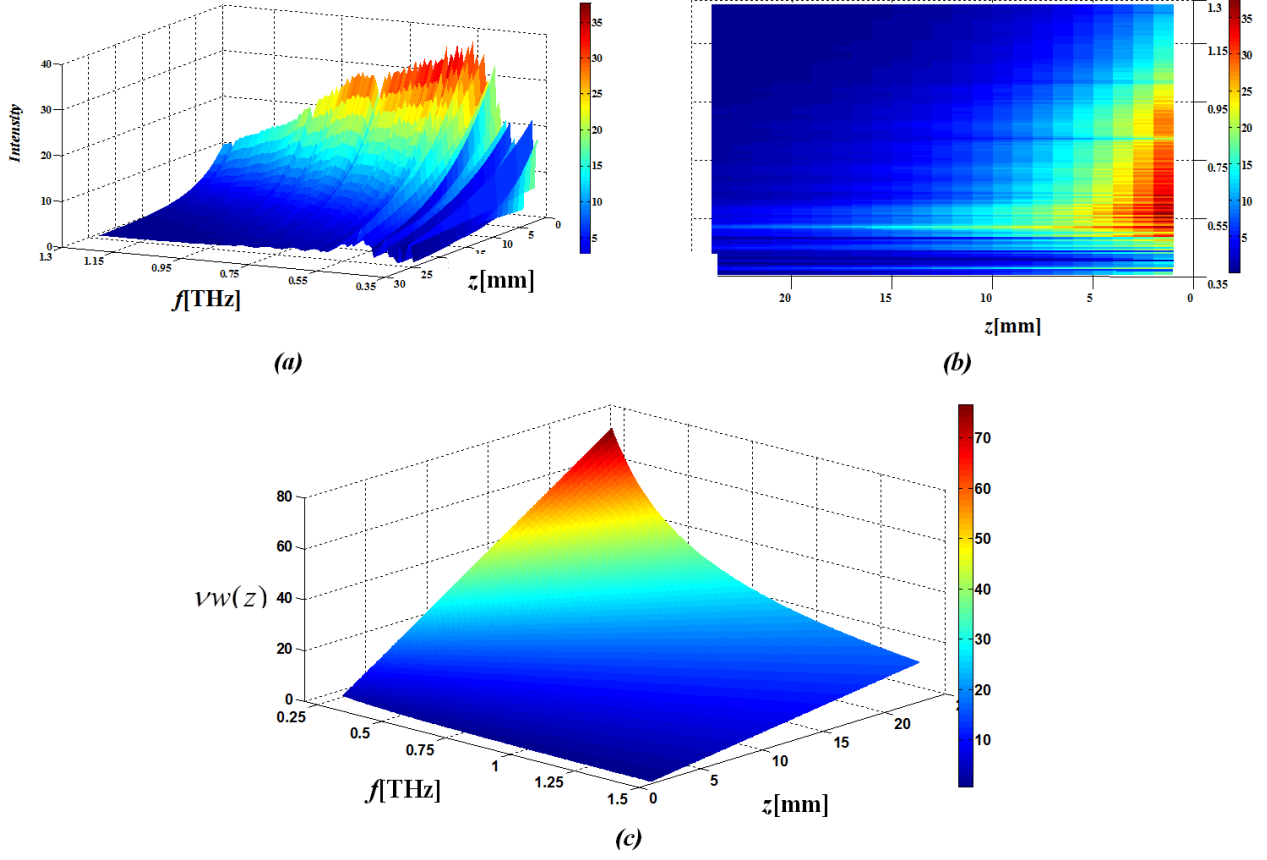


Figure 8 (a)-(b) divergence and (b) suppression of the beam over z - axis

4. RESULTS AND DISCUSSION

The high resolution X-ray image of the IC is shown in Figure-9 as the reference of comparison. The THz images after and before enhancement, are shown in Figure-10. Part (b) of this Figure illustrates the result of the deconvolution of the original THz image and the PSF, Equation-27, at $z=1$ mm. The inside bond wires are obviously appeared as a result. As shown in Figure-10-(b) the sizes of the inside wires of the IC and their gaps are consistent with the high resolution X-ray image. Figure-11 is the invert image of Figure-10-(b). This invert image is shown to have a better comparison with X-ray image; in X-ray the more the X-ray beam is attenuated the brighter the image obtains. As marked in Figure-11 the number of the inside bond wires are obtained accurately; 22 bond wires are showed up in Figure-11 as there are 22 bond wires in the X-ray image. As Equation-27 implies, the THz PSF also depends on z . Increasing z for 0.2 mm gives Figure-12-(b). This image seemed to be a better enhancement for the die part of the IC because at this z the die of the IC have the sharpest edges in the image. This implies that the correct z for the PSF is chosen. For Proving this theory the lateral X-ray image of the IC is obtained and shown Figure-13. The X-ray image indicates that the die is located 0.2 mm deeper inside the IC compared to the bond wires and thus the latter theory is proved. In case X-ray was not accessible, for proving the theory, this z location of the die and wires could be also measured with THz techniques in reflection mode¹². It is observed that the size of the die is acquired with the accuracy of ± 0.2 mm in the enhanced THz image. While in the original THz image more than 2.2 mm error is observed.

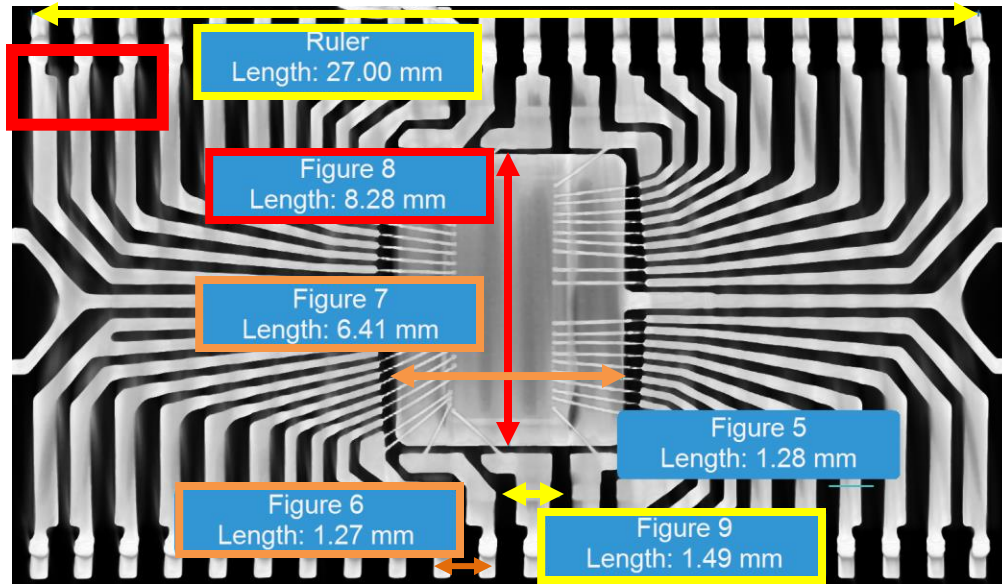


Figure 9 High resolution X-ray image

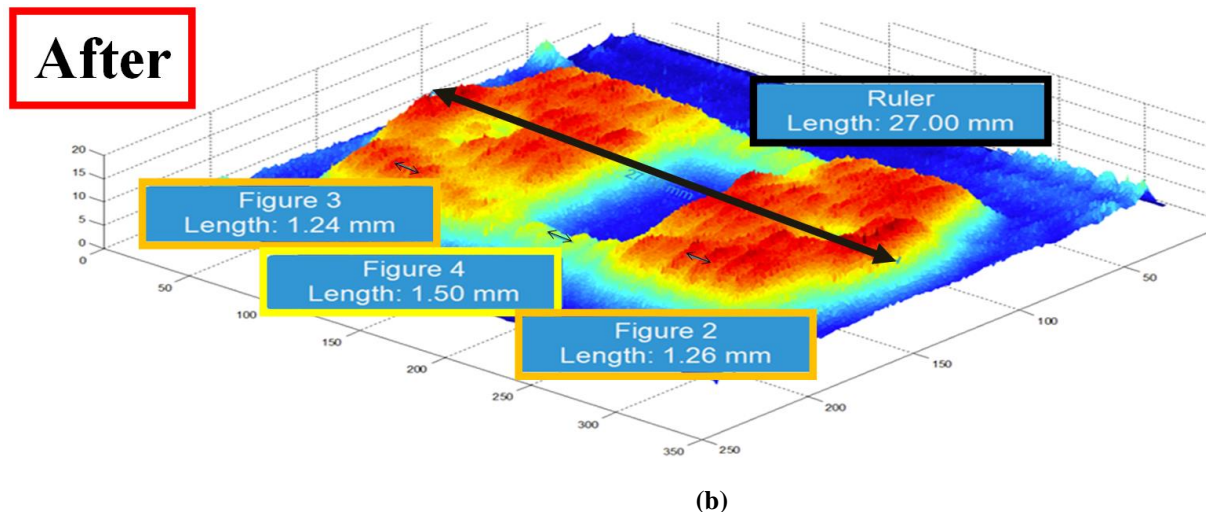
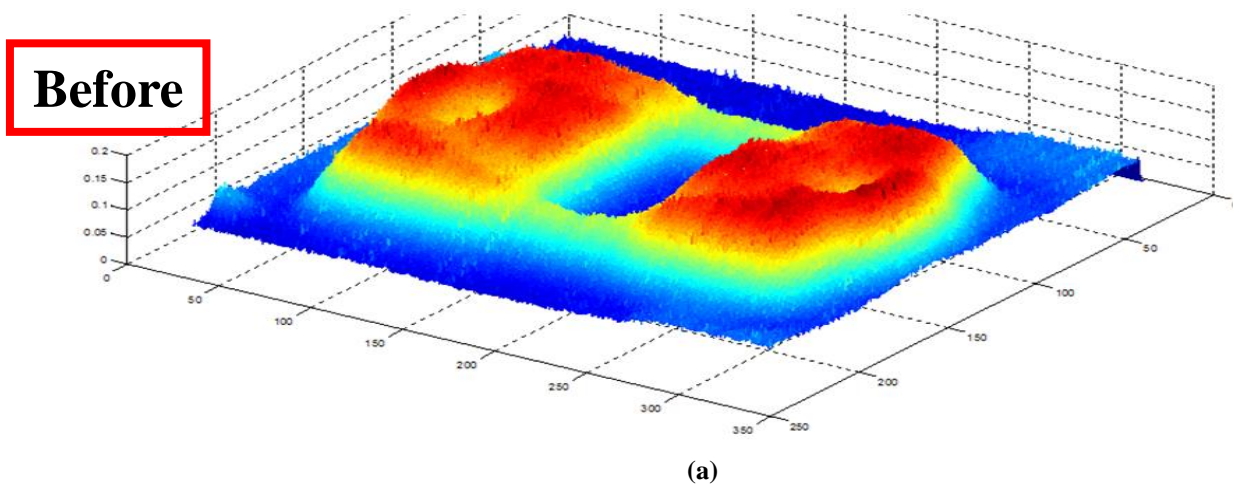


Figure 10 (a) THz image before enhancement; (b) THz image after enhancement: The inside bond wires are obviously appeared. Sizes of the inside bond wires of the IC and their gaps are consistent with the X-ray image. The obtained measurements are as accurate as 0.02 mm.

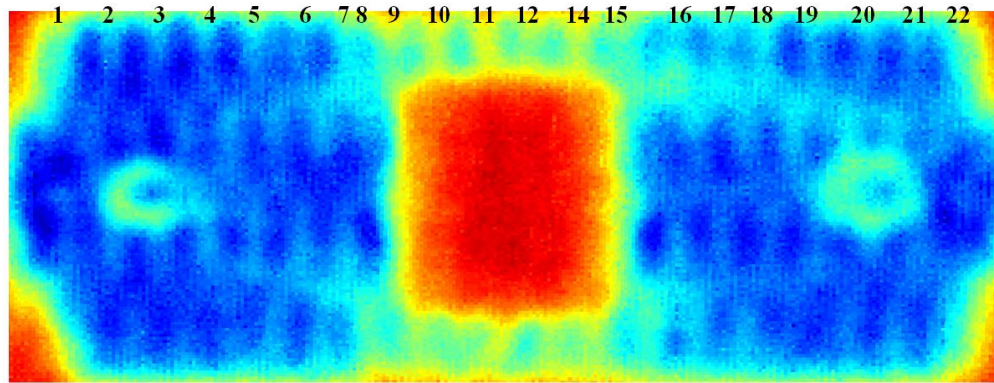


Figure 11 All the bond wires are appeared in the enhanced THz image

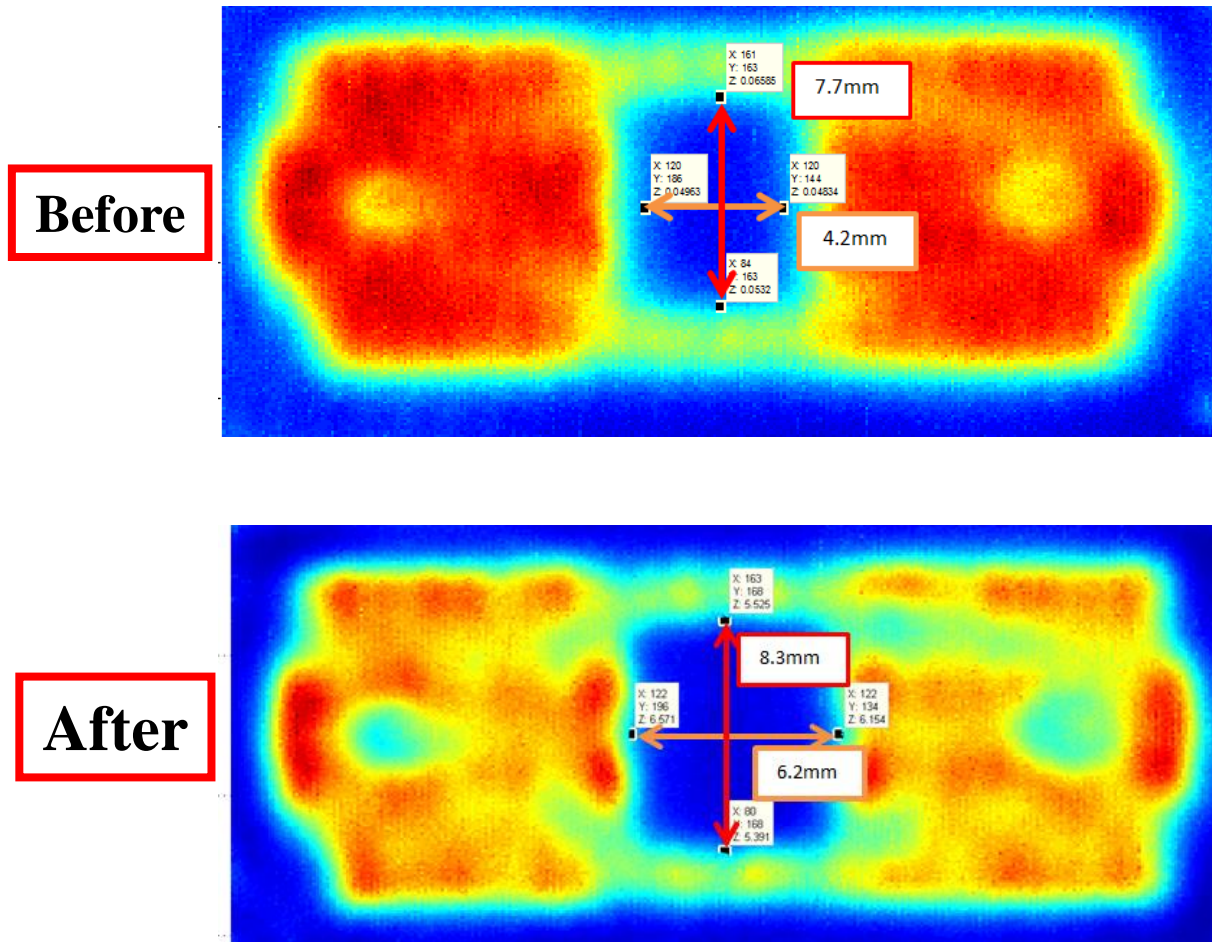


Figure 12 (a) THz image before enhancement; (b) THz image after enhancement: The shape and the size of the die are corrected. The accuracy of $\pm 0.2 \text{ mm}$ is achieved in the enhanced THz image. While in the original THz image more than 2.2 mm error is observed. Note: z for the die and bond-wires are not the same and thus, in this image bond-wires are not obvious. The lateral X-ray image confirms that the die is placed 0.2 mm deeper on z axis.

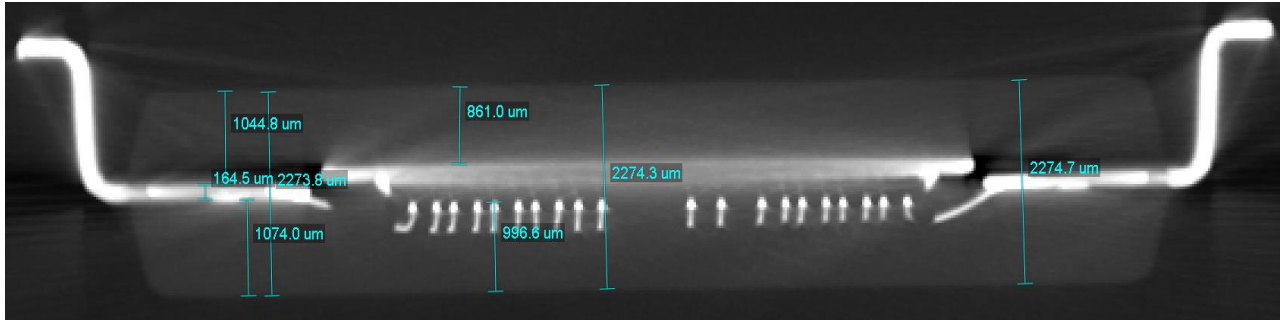


Figure 13 The lateral X-ray image indicates that the die is located 0.2mm deeper inside the IC compared to the bond wires.

A small portion of the images, $4.8 \times 1.1 \text{ mm}$, are cropped and shown in Figure-14. This portion is indicated by a red rectangle on top left side of Figure 9. The reconstructed image obviously indicates the location of the leads while the original image shows nothing meaningful.

The quality of the reconstructed image is measured by the structural similarity (*SSIM*) index and the mean squared error (*MSE*)^{37,38}. For this purpose the indicated portion of reconstructed THz image of Figure-10-(b) and the original THz image of Figure-10-(a), are given to *MSE* and the *SSIM* algorithm whereas the reference image is chosen to be the indicated section of high resolution X-ray image of Figure-9. The results of these quality measurements are shown in Table-I. As a result of the applying the developed approach here, the *MSE* is improved by %27.4 and *SSIM* by %50. Since the images which are given to *MSE* and *SSIM* were small, $48 \times 11 \text{ pixels}$, the values for *MSE* are small and the

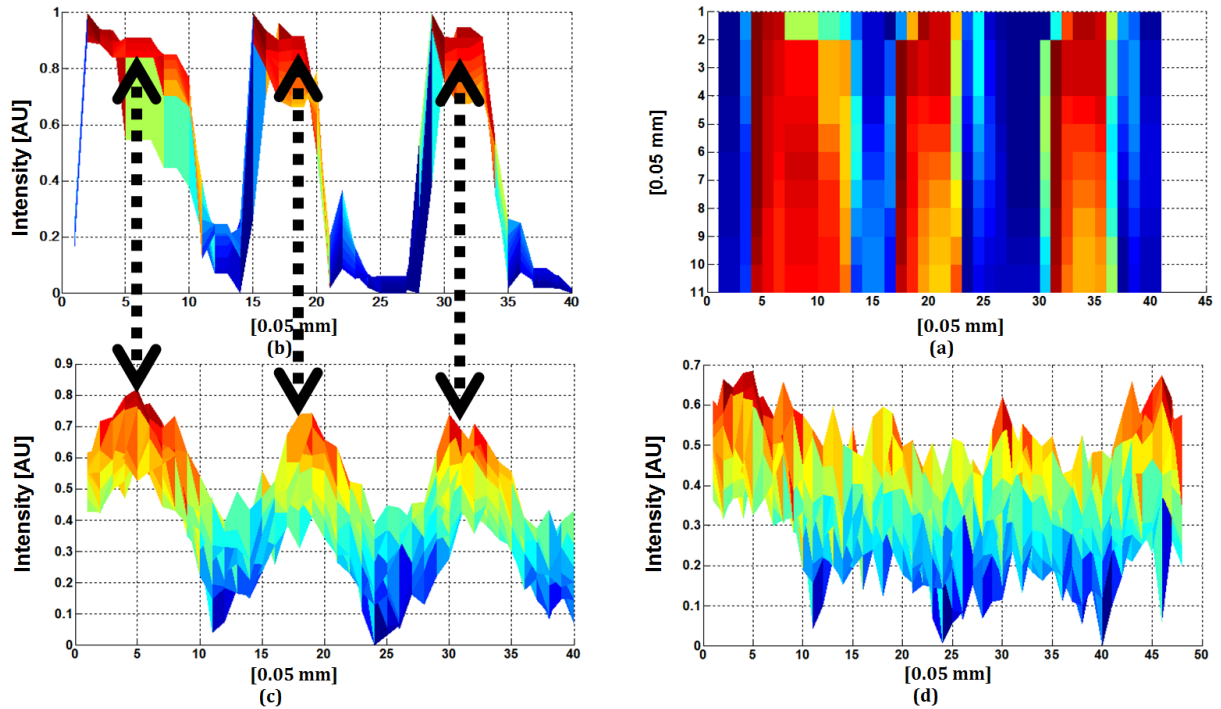


Figure 14 (a) Inverted X-ray image of three bond wires inside the IC; (b) The same inverted X-ray image of three leads inside the IC; (Note that Y axis is intensity this time) (c) THz Image Slice After Enhancement; (d) THz Image Slice Before Enhancement.

values for *SSIM* are relatively high. Thus, we defined *SSIM'* to be $(1-SSIM) \times 10^4$. For making comparisons, the percentage of the improvement is important here as Table-I indicates.

Table-I The improvement in quality of the reconstructed THz image compared to the original THz image

	SSIM'	MSE	Spatial Accuracy
Original THz image	136	0.1485	2.2 mm
Reconstructed THz image	68	0.1078	0.2 mm
Improvement	%50	%27.4	10 times higher

5. CONCLUSION

In this work the resolution of the THz images was improved. The hidden details in the THz images appeared as a result. For this aim, the THz PSF function was modeled. This PSF depends on many factors such as frequency of the beam, the depth of the beam in the object and absorption characteristics of the object. The THz images are obtained by raster scanning of the THz beam and the object. Consequently, reverse convolution of the THz beam and the THz image gives a higher resolution of the THz image. For realizing this theory, the reverse convolution of the THz PSF function and the THz image was achieved. Measurements of the sizes of the bond-wires and die of the IC in the enhanced THz image and comparing the values to the high resolution X-ray image proved that a considerable enhancement has achieved. Quality metrics such as MSE and SSIM were also calculated. It has been shown a great improvement in the quality of the THz images has achieved.

REFERENCES

- [1] Hejase, J. A., Member, S., Paladhi, P. R., Chahal, P. P., "Terahertz Characterization of Dielectric Substrates for Component Design and Nondestructive Evaluation of Packages," 1685–1694 (2011).
- [2] Hu, B. B., Nuss, M. C., "Imaging with terahertz waves," Opt. Lett. **20**(16), 1716 (1995).
- [3] Prince, J. L., Medical imaging signals and systems, Pearson Prentice Hall, Upper Saddle River, NJ (2006).
- [4] Stoik, C. D., Bohn, M. J., Blackshire, J. L., "Nondestructive evaluation of aircraft composites using terahertz time domain spectroscopy," Opt. Express **16** (2008).
- [5] Burford, N. M., El-shenawee, M. O., Neal, C. B. O., Olejniczak, K. J., "Terahertz Imaging for Nondestructive Evaluation of Packaged Power Electronic Devices" (2014).
- [6] Gerardin, S., Bagatin, M., Paccagnella, a., Grünmann, K., Gliem, F., Oldham, T. R., Irom, F., Nguyen, D. N., "Radiation Effects in Flash Memories," IEEE Trans. Nucl. Sci. **60**(3), 1953–1969 (2013).

- [7] [Pavan, P., Bez, R., Olivo, P., Zanoni, E., Member, S., "Flash Memory Cells — An Overview" \(1997\).](#)
- [8] Xin, W., Ren, S., Liu, D., Et.al., "SEB Hardened Power MOSFETs with High-K Dielectric," Nucl. Sp. Radiat. Eff. Conf. (2015).
- [9] Sung, S., "Electronic Thesis and Dissertations Los Angeles Terahertz Imaging and Remote Sensing Design for Applications in Medical Imaging A thesis submitted in partial satisfaction of the requirements for the degree Master of Science in Electrical Engineering by Sh," University of California (2013).
- [10] [Kawase, K., Ogawa, Y., Watanabe, Y., Inoue, H., "Non-destructive terahertz imaging of illicit drugs using spectral fingerprints," Opt. Express **11**\(20\), 2549 \(2003\).](#)
- [11] [Rivera, A., Mazady, A., Ahi, K., Anwar, M., "Growth dependent optical properties of ZnMgO at THz frequencies," Proc. SPIE 9483, Terahertz Physics, Devices, Syst. IX Adv. Appl. Ind. Defense, 94830X **9483**, 94830X \(2015\).](#)
- [12] [Ahi, K., Asadizanjani, N., Shahbazmohamadi, S., Tehranipoor, M., Anwar, M., "Terahertz characterization of electronic components and comparison of terahertz imaging with X-ray imaging techniques," . Proc. SPIE 9483, Terahertz Physics, Devices, Syst. IX Adv. Appl. Ind. Defense, 94830X \(May 13, 2015\), 94830K \(2015\).](#)
- [13] [Ahi, K., Asadizanjani, N., Tehranipoor, M., Anwar, A. F. M., "Authentication of electronic components by time domain THz Techniques," Connect. Symp. Microelectron. Optoelectron., Bridgeport, Connecticut, USA \(2015\).](#)
- [14] [Ahi, K., Asadizanjani, N., Shahbazmohamadi, S., Tehranipoor, M., Anwar, M., "THZ Techniques: A Promising Platform for Authentication of Electronic Components," CHASE Conf. Trust. Syst. Supply Chain Assur., Storrs, Connecticut, USA \(2015\).](#)
- [15] [Wietzke, S., Jansen, C., Rutz, F., Mittleman, D. M., Koch, M., "Determination of additive content in polymeric compounds with terahertz time-domain spectroscopy," Polym. Test. **26**, 614–618 \(2007\).](#)
- [16] [Coutaz, J., Duvillaret, L., "Influence of noise on the characterization of materials by terahertz time-domain spectroscopy," 452–461 \(2000\).](#)
- [17] [Blanchard, F., Doi, a., Tanaka, T., Hirori, H., Tanaka, H., Kadoya, Y., Tanaka, K., "Real-time terahertz near-field microscope.," Opt. Express **19**\(9\), 8277–8284 \(2011\).](#)
- [18] [Seo, M. A., Adam, A. J. L., Kang, J. H., Lee, J. W., Jeoung, S. C., Park, Q. H., Planken, P. C. M., Kim, D. S., "Fourier-transform terahertz near-field imaging of one-dimensional slit arrays : mapping of vectors," 11781–11789 \(2007\).](#)
- [19] [Adam, A. J. L., Brok, J. M., Seo, M. A., Ahn, K. J., Kim, D. S., Kang, J. H., Park, Q. H., Nagel, M., Planken, P. C. M., "Advanced terahertz electric near-field measurements at sub-wavelength diameter metallic apertures.," Opt. Express **16**\(10\), 7407–7417 \(2008\).](#)
- [20] [Natrella, M., Mitrofanov, O., Mueckstein, R., Graham, C., Renaud, C., Seeds, A., "Near-Field Probe Mapping of the THz Electric Field Distribution on Metallic Surfaces," Cleo 2013 **1**, CM2J.3, Osa, Washington, D.C. \(2013\).](#)
- [21] Adam, A. J. L., "Review of Near-Field Terahertz Measurement Methods and Their

Applications,” *J. Infrared, Millimeter, Terahertz Waves* **32**(8-9), 976–1019 (2011).

- [22] [Mueckstein, R., Mitrofanov, O., “Imaging of terahertz surface plasmon waves excited on a gold surface by a focused beam,” *Opt. Express* **19**\(4\), 3212–3217 \(2011\).](#)
- [23] [Coppa, a., Foglietti, V., Giovine, E., Doria, a., Gallerano, G. P., Giovenale, E., Cetronio, a., Lanzieri, C., Peroni, M., et al., “Active electric near field imaging of electronic devices,” *Infrared Phys. Technol.* **51**\(5\), 470–472 \(2008\).](#)
- [24] [Kiwa, T., Tonouchi, M., Yamashita, M., Kawase, K., “Laser terahertz-emission microscope for inspecting electrical faults in integrated circuits,” *Opt. Lett.* **28**\(21\), 2058–2060 \(2003\).](#)
- [25] [Nikawa, K., Yamashita, M., Matsumoto, T., Otani, C., Tonouchi, M., Midoh, Y., Miura, K., Nakamae, K., “Non-electrical-contact LSI failure analysis using non-bias laser terahertz emission microscope,” *Proc. Int. Symp. Phys. Fail. Anal. Integr. Circuits, IPFA* **2** \(2011\).](#)
- [26] Solomon, C., Breckon, T., *Fundamentals of Digital Image Processing* (2010).
- [27] [Jepsen, P. U., Keiding, S. R., “Radiation patterns from lens-coupled terahertz antennas,” *Opt. Lett.* **20**\(8\), 807–809 \(1995\).](#)
- [28] [Brown, E. R., “Fundamentals of Terrestrial Millimeter-Wave and THz Remote Sensing,” *Int. J. High Speed Electron. Syst.* **13**\(04\), 995–1097 \(2003\).](#)
- [29] Sagan, S. F., “Optical Systems for Laser Scanners,” 69–132.
- [30] [Yura, H. T., Rose, T. S., “Gaussian beam transfer through hard-aperture optics,” *Appl. Opt.* **34**\(30\), 6826–6828 \(1995\).](#)
- [31] [Fatholouloumi, S., Ban, D., Luo, H., Grant, P., Laframboise, S. R., Wasilewski, Z. R., Buchanan, M., Liu, H. C., “Beam Pattern Investigation of Terahertz Quantum Cascade Lasers,” *PIERS Online* **4**\(2\), 267–270 \(2008\).](#)
- [32] [Sagan, S., “Optical Systems for Laser Scanners,” \[Handbook of Optical and Laser Scanning, Second Edition\], CRC Press, 69–132 \(2011\).](#)
- [33] [Hansch, T. W., “Repetitively Pulsed Tunable Dye Laser for High Resolution Spectroscopy,” *Appl. Opt.* **11**\(4\), 895–898 \(1972\).](#)
- [34] [Hejase, J. a., Rothwell, E. J., Chahal, P., “Self-calibrating technique for terahertz time-domain material parameter extraction,” *J. Opt. Soc. Am. A. Opt. Image Sci. Vis.* **28**\(12\), 2561–2567 \(2011\).](#)
- [35] [Duvillaret, L., Garet, F., Coutaz, J. L., “A reliable method for extraction of material parameters in terahertz time-domain spectroscopy,” *Sel. Top. Quantum Electron. IEEE J.* **2**\(3\), 739–746 \(1996\).](#)
- [36] [Jin, Y., Kim, G., Jeon, S., “Terahertz Dielectric Properties of Polymers,” *J. Korean Phys. Soc.* **49**\(2\), 513–517 \(2006\).](#)
- [37] Wang, Z., Bovik, A. C., “Mean Squared Error: Love It or Leave It ?,” *IEEE Signal Process. Mag.* **26**(January), 98–117 (2009).
- [38] Wang, Z., Bovik, A. C., Sheikh, H. R., Simoncelli, E. P., “The SSIM Index for Image Quality Assessment,” <<https://ece.uwaterloo.ca/~z70wang/research/ssim/>>.